More than Spicy, Moringa oleifera as a Feedstock for Functional biochar@ZnO

Radhia Msaadi *, Arvind K. Bhakta *, Wafa Sassi, Mengqi Tang, Ronald J. Mascarenhas, Zineb Mekhalif, Salah Ammar, MOHAMED CHEHIMI *

Posted Date: 7 October 2024

doi: 10.20944/preprints202410.0485.v1

Keywords: Biocarbon; ZnO; Moringa oleifera; Environmental remediation; Circular-bioeconomy; Waste-to-wealth

 doi:10.20944/preprints202410.0485.v1

Article

More than Spicy, *Moringa oleifera* as a Feedstock for Functional biochar@ZnO

Radhia Msaadi [1,*], Arvind K. Bhakta [2,*], Wafa Sassi [1], Mengqi Tang [2], Ronald J. Mascarenhas [3], Zineb Mekhalif [4], Salah Ammar [1] and Mohamed M. Chehimi [2,*]

[1] Faculté des Sciences, Laboratoire de Recherche Matériaux, Electrochimie et Environnement LRMEE (LR24ES18), Université de Gabès, 6000, Gabès, Tunisia
[2] Université Paris Cité, CNRS, ITODYS (UMR 7086), 75013 Paris, France.
[3] St. Joseph's University (Autonomous), Department of Chemistry, 560 027 Bengaluru, India.
[4] CES, NISM, University of Namur, B-5000 Namur, Belgium.
* Correspondence: mohamed.chehimi@cnrs.fr (MMC); radhiaradhia44@gmail.com (RM), arvindk.bhakta@gmail.com (AKB)

Abstract: Water treatment is one of the most research-challenging areas, and continuously requires the development of efficient sustainable materials for catalytic total mineralization of organic compounds. Herein, *Moringa oleifera* biomass was converted to "black gold" biochar loaded with ZnO nanoparticles (MOFB@ZnO) by slow pyrolysis, at 500 °C under an inert atmosphere, (MOFB@ZnO). This composite catalyst was used for the total degradation of Congo Red, a model organic pollutant. SEM confirmed the uniform distribution of ZnO nanoparticles, while XPS and XRD indicated the presence of ZnO, primarily in the wurtzite crystalline structure. Optimization was conducted using the central composite design (CCD) method and STATISTICA 12.0 software. The composite catalyst was applied in the electrochemical degradation of Congo Red dye, using a platinum anode and a carbon felt cathode to generate H_2O_2 from O_2 reduction. The ZnO-decorated *Moringa oleifera* biochar catalyst permitted to achieve of 98% removal of total organic carbon in less than 6h. It is 10-fold more efficient than pristine biochar and can be recycled up to 4 times without any significant loss. The process is highly efficient producing sustainable low-cost catalysts for water purification from organics, and contributes to sustainable chemical processes therefore addressing SDGs 6, 9, and 13.

Keywords: biocarbon; ZnO; *Moringa oleifera*; environmental remediation; circular-bioeconomy; waste-to-wealth

1. Introduction

In the past decades, carbon nanotubes and graphene followed by other carbon allotropes have dominated the research field [1]. The realization that green chemistry is an important brick in the quest for sustainable development and circular bioeconomy, has led to ever-increasing attention to biomass-derived carbon materials [2]. They can be mostly classified into biochar or hydrochar [3], and to a lesser extent to the emerging ionochar [4]. Biochar is produced by a thermochemical process called pyrolysis (in a limited or no oxygen environment) [5]. Biochar can also act as a precursor for making other carbon allotropes such as graphene [6]. They possess peculiar properties such as surface charge, water holding capacity, surface area, high porosity, surface functionalities (-COOH, -OH, -R-OH, C=O), cation exchange capacity, nutrient exchange site, carbon sequestration, high pH, nutrients, salinity, etc [7,8], make them potential candidates for many applications. Biochars exist in various shapes, sizes, and porosity depending on the process, precursors, and pyrolysis conditions [9]. They are considered as substrates for green infrastructure [10]. They are successfully applied in soil remediation [11,12], wastewater treatment [13,14], fuel [15], batteries [16], supercapacitors [17,18], and paints [19], to mention a few. Biochar is found to be beneficial for the growth, productivity, and improved physiological performance of crops even under toxic environments [20]. Henceforth, biochar is one of the key materials to address sustainable environmental issues [21–25].

 doi:10.20944/preprints202410.0485.v1

In the current world, water pollution is becoming a great challenge. There are different reasons for water pollution including the dyes coming from different industries [26]. One such dye is Congo red which belongs to the class of azo dyes (compounds containing diazotized amine connected to an phenol or amine) [27,28]. They are used in textile industry, pH indicator, pharmaceuticals and tissue staining. They are mutagenic, carcinogenic, phytotoxic, increase chemical oxygen demand (COD), and make surface water unaesthetic [29]. Therefore, an efficient treatment for the removal of dyes is essential for environmental remediation.

Zinc oxide (ZnO) nanoparticles exhibit unique catalytic, electrical, UV-absorbing, optoelectronic properties and photocatalytic properties which are found very efficient in pollutant removal [30–35], electrochromic applications [36], temperature sensors [37], enhanced corrosion stability [38], CO_2 hydrogenation to methanol [39], UV-light emitters [40], microbial desalination cells [41], to mention few. Zinc oxide also plays a very important role in the ceramic industry [42].

In the literature, there are some works on biochar and ZnO related to Congo Red pollutants removal such as green pea peels biochar/ZnO (biosorption) [43], ZnO/cotton stalks biochar (adsorption) [44], and ZnO-green seaweed biochar (photocatalysis) [45]. Even just biochar is also used to remove CR through adsorption [46]. However, the fate of CR after adsorption is not clear and other methodologies where dyes are degraded, have used lengthy processes to synthesize catalysts.

The characteristics of biochar change depending on the biomass sources, which is due to variations in cellulose, hemicellulose, and lignin composition. In the race for biochar, one such biomass is *Moringa oleifera.* It belongs to the genus Moringa and family Moringaceae, commonly known as 'drumstick tree' or 'horseradish tree' [47]. There are only a few works on the utilization of *M. oleifera* biochar for water treatment such as the removal of arsenite arsenate ions [48], fluorides [49], crystal violet [50], and methylene blue [51]. In the context of waste water treatment, electrochemical methods are preferable over other techniques because of fast, cost-effectiveness and good efficiency. For example, Pd supported corn-husk biochar was used for electrochemical Cr (VI) reduction [52]. Modified biochar with $ZnCl_2$ and $FeCl_3$ for electrochemical degradation of nitrobenzene [53], to cite few. Concerning, organic pollutants, biochar loaded with nanocatalysts is scarcely used in electro-Fenton applications [54,55], but the reported methods are long and tedious, and concern only iron as the immobilized catalyst, in contrast to this work which follows a simple route for making biochar loaded with nanocatalyst for the electrochemical degradation of organic pollutant.

This study explores the feasibility of using Moringa biochar and ZnO-modified biochar for the electro-degradation of Congo red, an azo dye, from aqueous solutions. The research optimizes key parameters using central composite design (CCD) to enhance Congo red treatment efficiency. It investigates the capacities of Congo red degradation on both biochar and biochar-ZnO composite, characterizes the properties of the modified biochar, and examines various degradation mechanisms including kinetic studies and reusability. SEM, XRD, and XPS investigations are employed to elucidate the molecular interactions of the Congo red dye, complementing experimental findings. The study highlights the superior degradation performance and interaction dynamics of ZnO-modified biochar compared to unmodified biochar, emphasizing the role of electrolysis in enhancing degradation mechanisms for efficient wastewater treatment applications.

2. Materials and Methods

2.1. Chemicals

All the aqueous solution used in this work are made using double distilled water. Moringa Oleifera powder (MOF) was obtained from Tunisia. The waste generated from the seed pods were dried and ground. Zinc acetate (99.99%) was procured from Sigma-Adrich.

2.2. Apparatus

GeminiSEM 360 was used to understand the surface morphology. This instrument was operated at accelerating voltage 5kV and current 30μA with a working distance of 8-9. XRD characterization was performed on X'Pert PRO PANalytical instrument maintained at tube current of 40 mA and

 doi:10.20944/preprints202410.0485.v1

operating voltage of 40 kV. Thermo Scientific K Alpha + instrument, fitted with Al Kα source (hν = 1486.6 eV) was used to perform XPS analysis with pass energy 200 eV for survey scans, and 80 eV for the acquisition of the high-resolution spectra. Raman characterization was done on Horiba HR 800 spectrometer (Kyoto, Japan). TGA characterization was performed using an HP DSC SETARAM SENSYS EVO (Caluire, France) in the presence of air (29°C to 890°C), at a heating rate of 10 °C/min.

2.3. Synthesis of ZnO-Coated Biochar

A wet impregnation technique was used to create ZnO nanoparticles [56]. Firstly, 1.5 g of *Moringa oleifera* powder (MOF) was mixed with 10 ml solution containing 275 mg Zinc acetate, dried and ground. Further, they were subjected to pyrolysis as follows: Type of Method- P10 KOH free, Ramp- 20 °C / min, Temperature - 500 °C, Residence time – 1 hour, and cooling time-1 hour (Figure 1).

Percentage yield = 0.5901g / 1.5869g x 100 = 37.19 %

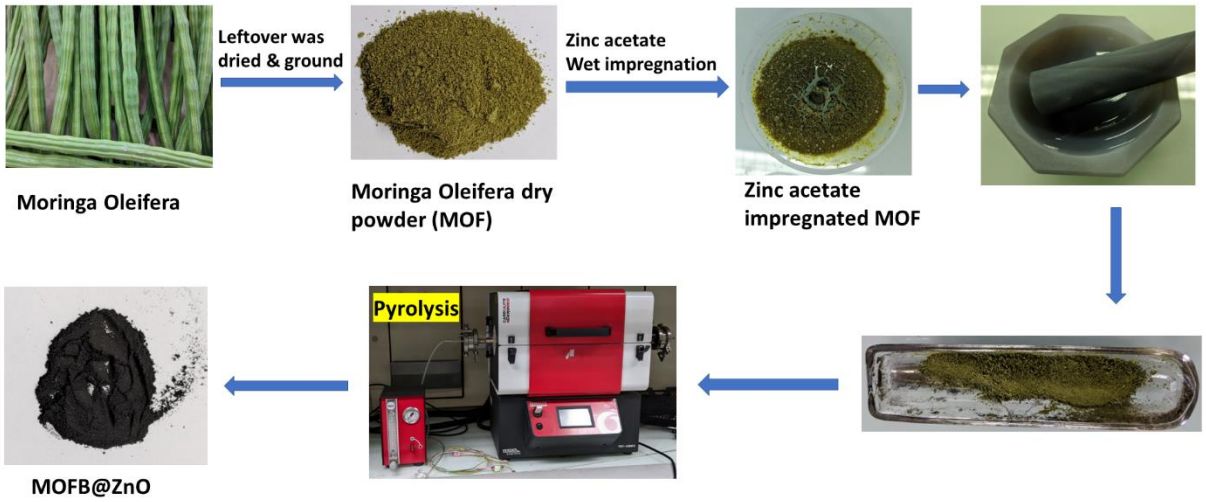

Figure 1. Steps involved in the synthesis of biochar@ZnO.

2.4. Electrochemical Degradation

The electrochemical process unfolded within a single, unpartitioned cylindrical container containing 250 mL of vigorously stirred solutions, facilitated by a magnetic stir bar. The anode, crafted from cylindrical Pt mesh, measured 4.5 cm in height and featured an internal diameter of 3 cm. A 3D carbon felt component (dimensions: 10 cm * 3 cm * 0.5 cm, Carbon-Lorraine, Paris, France) serves as the cathode. The anode consistently maintained its central position within the electrochemical cell, surrounded by the cathode, which covered the inner wall of the cell. A continuous supply of air to the solution initiated 20 minutes before the start of electrolysis and maintained throughout, was sustained at a rate of 1 L/min. The electrochemical degradation process involved solutions containing 20 mg/L of congo-red in a 0.05 M Na_2SO_4 solution, with a biochar-ZnO dosage of 0.2 g/L. To attain a solution pH of around 3, a small quantity of 2 M sulfuric acid was added. All experiments were conducted in a light-free environment to prevent any photolytic effects. The current-voltage remained constant at 300 mA, and the catalyst was effortlessly retrieved after the treatment through filtration.

Design of experiments and optimizing the variables were carried out by central composite design (CCD). The data were analyzed using STATISTICA Software, and the CCD model.

3. Results and Discussions

3.1. ZnO Modified Biochar Characterizations

 doi:10.20944/preprints202410.0485.v1

The surface morphology of the synthesized materials was investigated using FESEM techniques. Low- and high-resolution SEM spectra (Figure 2) clearly indicates the presence of uniform ZnO nanoparticles, homogeneously distributed over the biochar surface. The nanoparticles size range is 40-75 nm approximately. They are mostly spherical in shape.

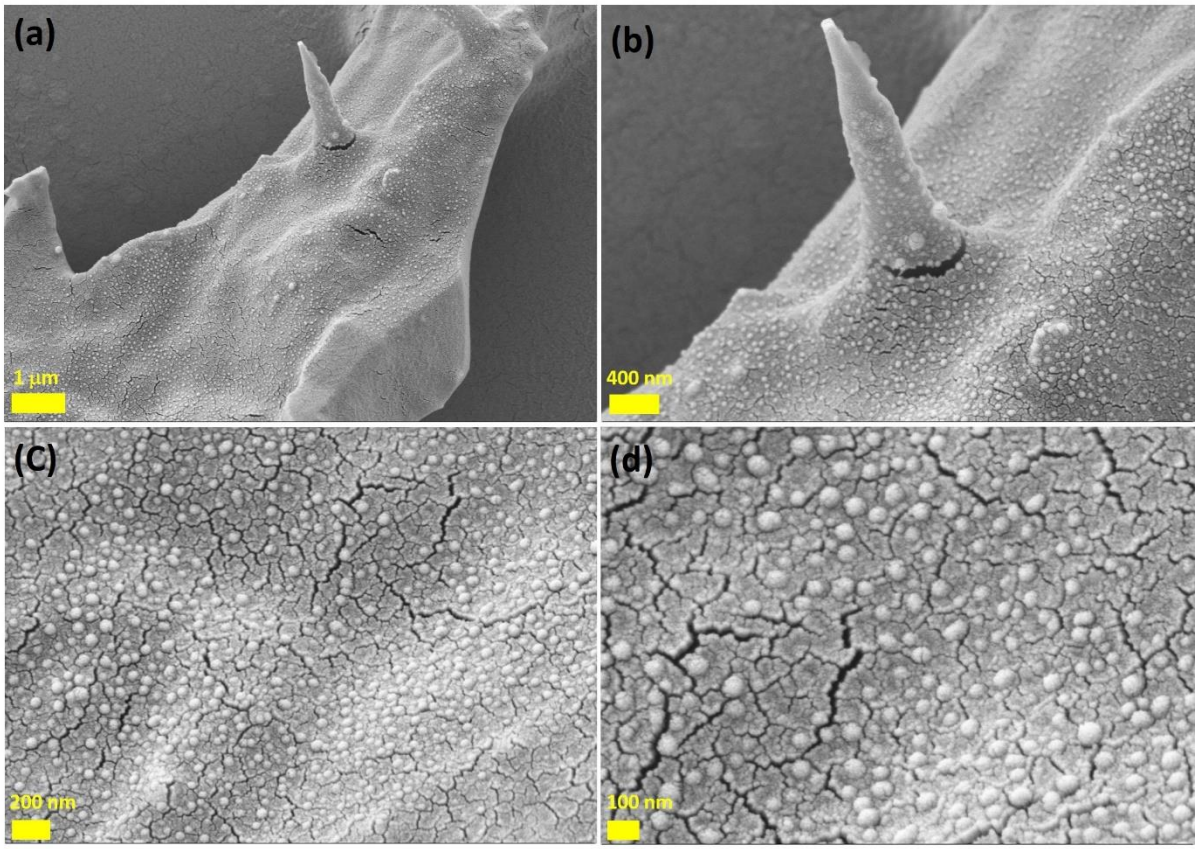

Figure 2. FESEM images of MOPB@ZnO at different magnifications.

Literature have suggested that ZnO can exist in different shapes and sizes on the surface of biochar. For Example, ZnO nanorods [57], flowers [58], spheres [59], etc. The pyrolysis temperature plays a major role in tunning the shape and size of ZnO nanoparticles on the surface of biochar [60]. It should be noted that there was no aggregation of ZnO particles, indicating that nucleation primarily occurred on the external surface [61]. Furthermore, the oxygen-containing functional groups on the biochar surface served as nucleation sites for the ZnO nanospheres, resulting in the independent formation of micro-cracks around each ZnO sphere on the biochar surface. The micro-cracks can be attributed to several factors; Differences in thermal expansion coefficients between ZnO and biochar may induce mechanical stresses during heating and cooling cycles, leading to cracks or internal stresses generated during nanoparticle growth reactions or dehydration processes which can also cause cracks [62]. In our case, it seems that interactions between the biochar and ZnO nanospheres, as well as variations in particle concentration or distribution, may further exacerbate these stresses and contribute to the formation of micro-cracks as mentioned by Ozturk et al. [63].

The crystalline phase was analyzed using X-ray diffraction (Figure 3).

 doi:10.20944/preprints202410.0485.v1

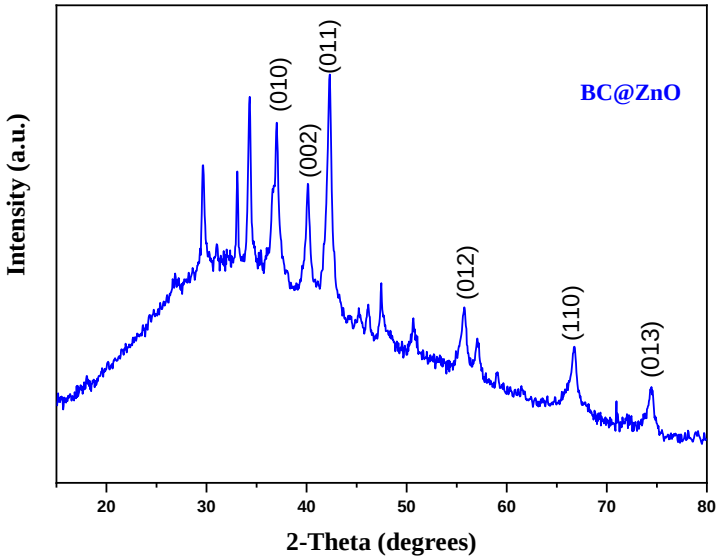

Figure 3. XRD Pattern of MOFB@ZnO.

The presence of sharp and intense peak is a clear indication of ZnO nanocrystals. The peaks at 2θ = 37.6, 40.2, 42.3, 55.8, 66.8 and 74.5, corresponds to the reflection from the plane (010), (002), (011), (012), (110), and (013) respectively. This observation suggested that ZnO formed with a hexagonal wurtzite structure, aligning with literature on ZnO obtained through pyrolysis with organic bases [64–66]. No impurity peaks were detected in the XRD patterns of MOFB@ZnO. Moreover, carbon was not visible in the XRD patterns, likely due to its minimal amount and amorphous nature. The hydrozincite phase of ZnO was not detected in this XRD patterns Indeed, such phases are usually obtained at low pyrolysis temperature (80°C) via both hydrothermal and chemical precipitation methods [67,68]. The crystallite size of the nanoparticles was calculated using Debye Scherrer equation from the strongest diffraction peak (011) as follows:

$D = K\lambda / \beta \cos\theta$ (Eq. 1)

Where, k represents Scherrer constant, λ = wavelength, β = Full width at half maximum. The average crystallite sizes for ZnO were determined to be 25 nm. According to Dumbrava et al. [45], the crystallite sizes for pure ZnO samples were either 35.86 nm or 31.67 nm regardless of the synthesis method. As expected, a higher synthesis temperature resulted in greater crystallinity and a decrease in crystallite size for the ZnO modified biochar sample, which is consistent with other studies showing that higher reaction temperatures in hydrothermal treatments decrease nanoparticle size for various nanomaterials [67,68]. The lower values for ZnO-based nanospheres in our study compared to other ZnO modified biochar are due to the presence of long hydrocarbon chains. Comparing the XRD patterns of MOFB@ZnO composites with those of pure ZnO existing in several literature and XRD data base may show difference in the intensity ratio of the three most intense peaks, suggesting a different distribution of atoms among the three diffraction planes. Some researchers [67,68] suggest that minor differences in peak positions (2θ values) and similar interplanar distance (d) values may indicate that carbon atoms were not incorporated into the ZnO lattice.

The elemental analysis and oxidation state of Zn were studied using XPS analysis. The survey spectrum (Figure 4a) reveals the presence of different elements such as Zn (4.95 %), S (0.73%), N (2.91%), C (67.57 %), O (19.42%), Si (0.59%), Ca (2.25%), Na (0.43%), Mg (0.40%) and Cl (0.76%). The contribution of sulphate can be due to Fucan [69]. The presence of Zinc in the oxide form [70] is confirmed by the Figures 5b, c . The modified Auger parameter α' = 2009.9 eV, matching values reported elsewhere [71,72] . Even though there is the presence of sodium and chloride, there is not any adverse effect on the catalytic effect of MOFB@ZnO. The presence of zinc (4.95 %) and oxygen (19.4%), in significant quantity indicated the high loading of ZnO on the biochar support.

 doi:10.20944/preprints202410.0485.v1

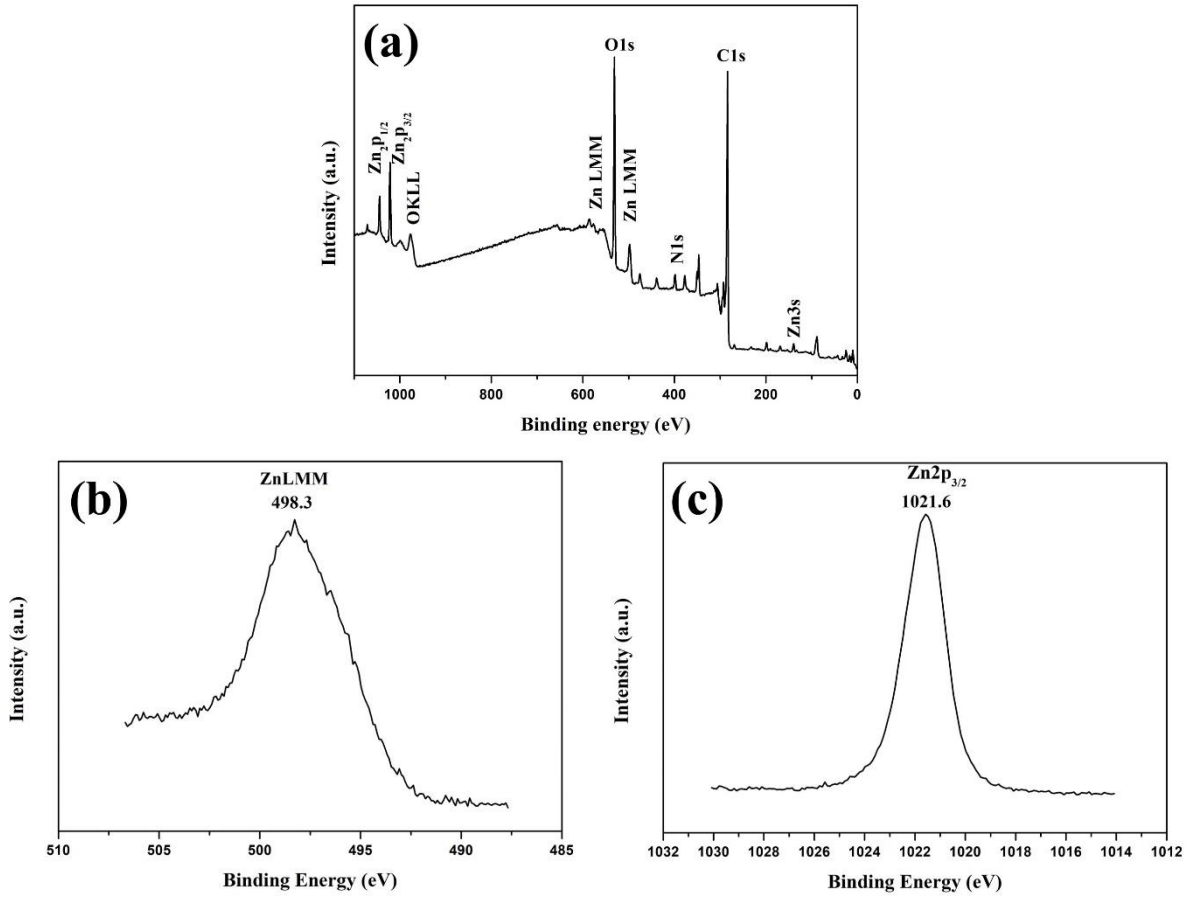

Figure 4. XPS survey spectra, ZnLMM, and Zn2p3/2 of MOFB@ZnO.

 doi:10.20944/preprints202410.0485.v1

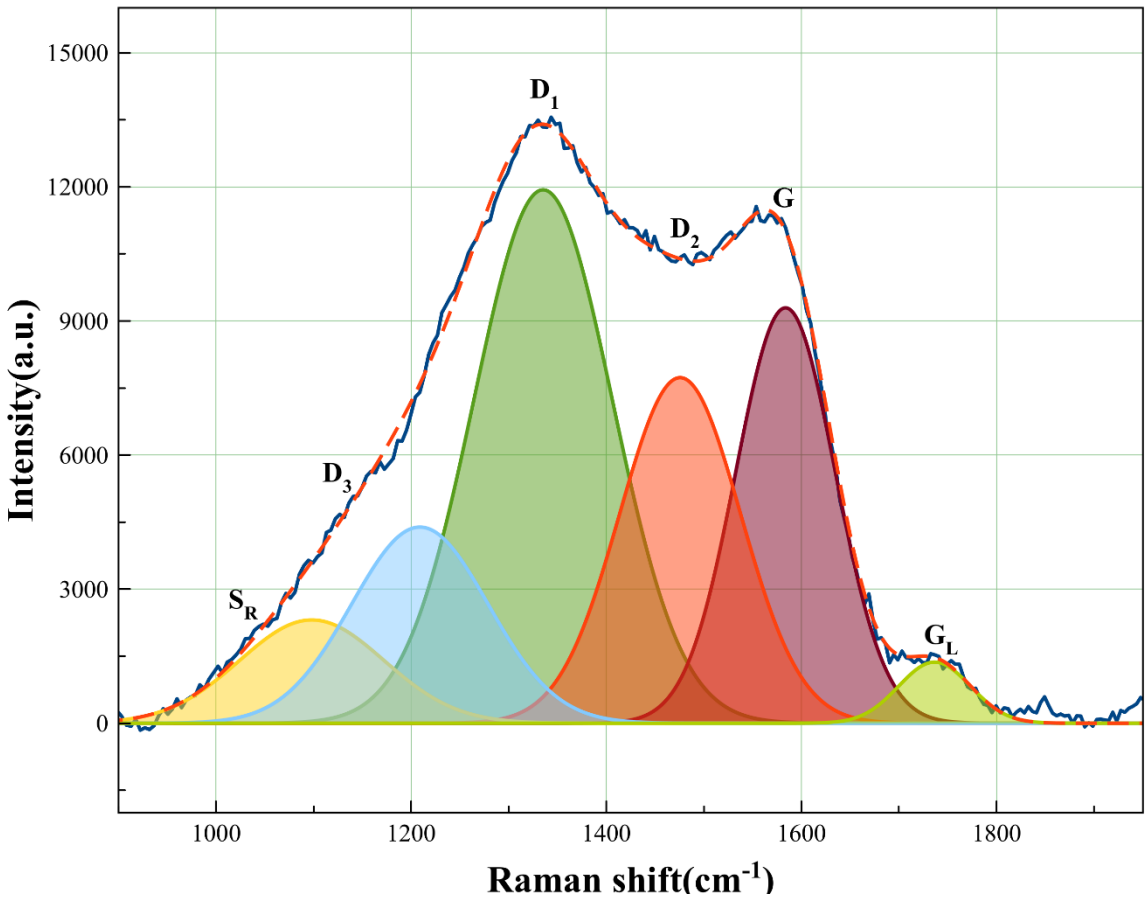

Figure 5. Raman peak fitting of MOFB@ZnO.

The Raman study was performed to understand the purity and quality of synthesized nanocomposite. The Raman peak fitting is reported in Figure 5. The Raman D/G band was fitted with 6 components: S_R (hydrogen circulation along periphery), D_3 (alkyl- alkyl ether), D1 (defects and heteroatoms), D_2 (sp^2-c), G (degree of graphitization) and G_L (carbonyl function) [73]. D/G ratio is greater than 1 for the fact that high loading of ZnO nanoparticles creates defects in the biochar. Nevertheless, they also provide higly active sites for catalytic reactions.

3.2. Thermal Analysis

The thermos gravimetric analysis (TGA) was performed to understand the thermal stability of the materials [74]. The thermal decomposition of MOFB@ZnO (Figure 6) can be divided into three stages [75]. Stage 1 (60 °C- 181°C), corresponds to water vaporization. After this temperature until 410 °C, devolatilization and dehydrogenation occurs. This stage also shows the combustion of biochar itself. After this stage, the mass remains constant as remained ZnO has high melting temperature. The mass loss proceeds until ~730 °C, indicating relative robust system, compared to ZnO-loaded spent coffee biochar [76]. Such a stability is possibly due to biochar-O-Zn interface [76].

The differential scanning calorimetry (DSC) curve (Figure 6b) is on a positive scale indicating the process is exothermic. Derivative thermogravimetry (DTG) plot as shown in Figure 6c has revealed that T_{mwl} (temperature of maximum weight loss rate) is 420 °C.

 doi:10.20944/preprints202410.0485.v1

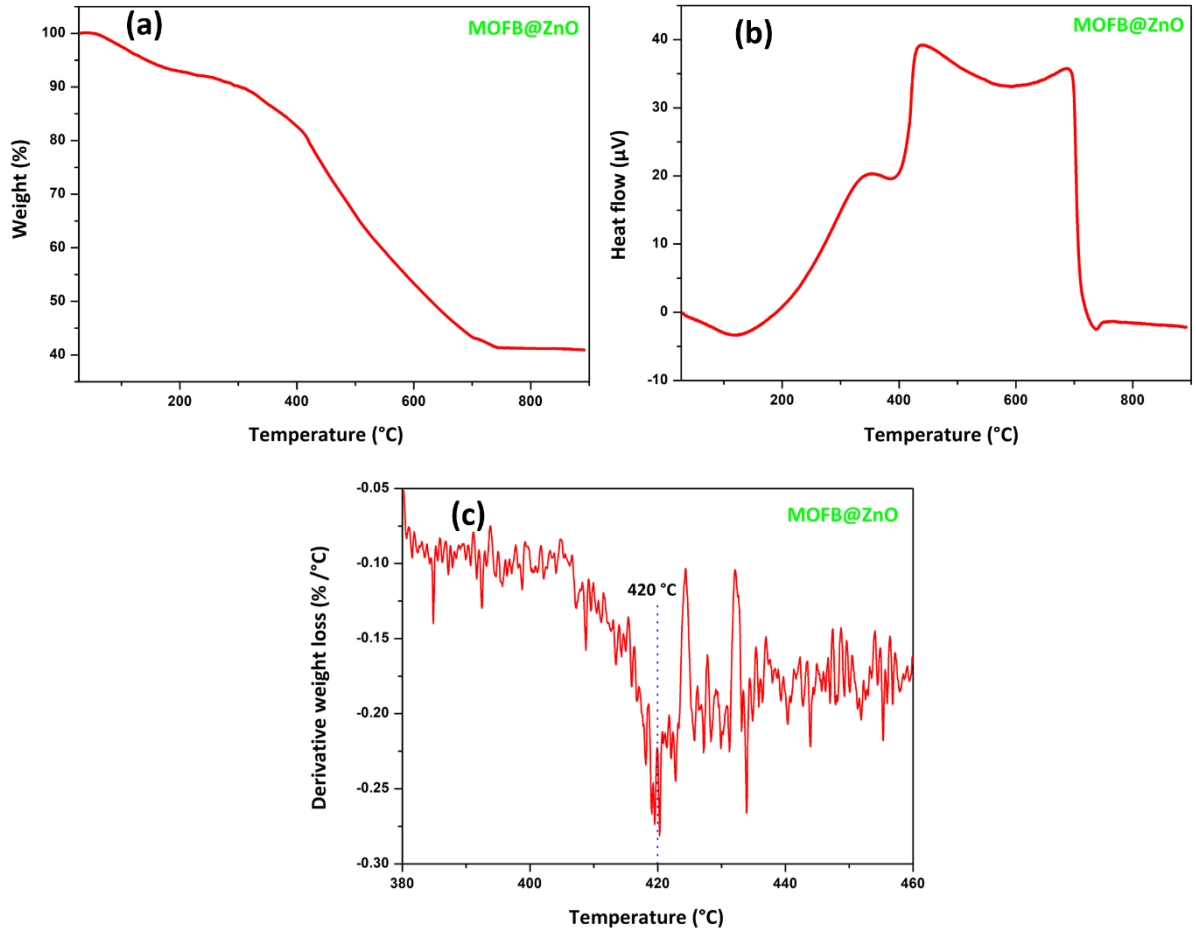

Figure 6. (a) TGA, (b) DSC, and (c) DTG of MOFB@ZnO.

3.3. Electrochemical Degradation of Congo Red

3.3.1. Optimization and Prediction

The experimental field shown in Table 1, was a resume from many research [77] dealing with dyes electro-degradation using biochar-based material.

Table 1. Experimental field for studied factors.

Factors	Code	(- δ)	(-1)	(0)	(+1)	(+ δ)
Electrolysis time t_c (min)	X_1	28	120	240	360	452
Dye concentration C (mg/L)	X_2	12	20	30	40	48
Electrolysis current I (mA)	X_3	124	200	300	400	476

The δ is the code of rotatability and orthogonality for the adopted CCD design and it is calculated using the Eq.2[78]

$$\boldsymbol{\delta} = \sqrt[4]{\frac{\boldsymbol{n_f} \times (\sqrt{\boldsymbol{n}} - \sqrt{\boldsymbol{n_f}})^2}{\boldsymbol{4}}} \text{ (Eq. 2)}$$

When, n_f is the number of runs proposed by the factorial plan (Eq.3) and n is the total number of runs proposed by the CCD model, explained as the Eq.4 [78,79]

$$\boldsymbol{n_f = l^3} \text{ (Eq. 3)}$$

$$\boldsymbol{n = n_f + l \times 3 + c \times r} \text{ (Eq. 4)}$$

When, *l* is the level, *c* is the number of model centers, and *r* is the number of repetitions. In our case, *n* and the code δ are 16 runs and 1.69, respectively. The equivalency between design codes and

 doi:10.20944/preprints202410.0485.v1

factor values was presented elsewhere [80]. The optimum conditions for the dye's degradation generated by the software are present in Figure 7.

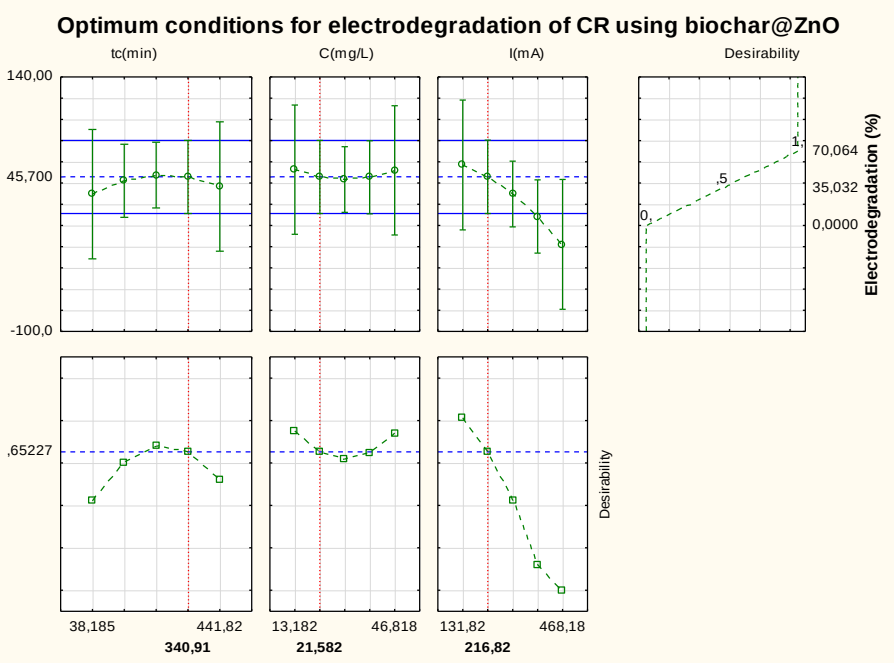

Figure 7. Optimum conditions of the CR electro-degradation using MOFB@ZnO.

The adsorption yields' ranges recorded were from 0 to 70% for the CR dye. We could conclude herein that the MOFB@ZnO seems have catalytic properties. The optimum conditions generated by the software were 341 min, 22 mg/L and 217 mA for the contact time, dye concentration and applied current, respectively. At this stage, the high value of applied current 217 mA as adequate current for a better CR degradation would propose a slow kinetic process.

The degradation yield of CR at these optimum conditions were exactly 70.06 %.

The mathematical prediction model generated by the software for the CR dye is present in Eq.5:

$$Y_{CR}\ (\%) = 35.03 + 2.22\ x_1 + 0.11{x^2}_1 - 0.081x_2 + 0.01{x^2}_2 + 1.86\ x_3 + 0.02\ {x^2}_3 + 0.01x_1x_2 + 0.03\ x_2x_3 + 0.42x_1x_3 \pm 0.21 \quad \text{(Eq. 5)}$$

The detailed significance of each parameter was presented elsewhere [79]. Accordingly, to Eq.4, the contact time and applied current density seem to have positive effect on the adsorption yield. This is due to the positive coefficients of main effect recorded. Additionally, the negative value of dye concentration's coefficient was inversely proportional to the response. This would confirm that the electrodegaradation process is spontaneously favorable [80].

The regression coefficient and the superposition between experimental data and the predicted values calculated using Eq.4 are presented in Figure 8.

 doi:10.20944/preprints202410.0485.v1

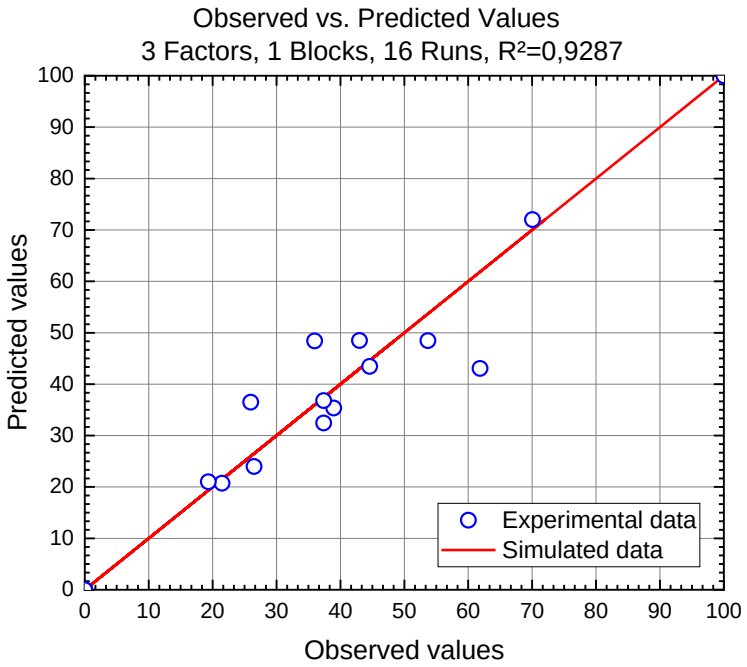

Figure 8. Linearity test between predicted and observed response values of the CR electrodegaradation yield using MOFB@ZnO.

The recorded R^2 for simulation was 0.93 for the CR. This would proving the correct choice of the CCD matrix for the electro-degradation process modelling. Another interesting information could be seen in the Figure 8; The CR electrodegradation yields accumulation was between 20 to 70 %. This would confirm that MOFB@ZnO catalyst still efficient for CR dye treatment as suggested above. In all subsequent experiments, we maintained the optimal conditions constant except for the parameter under study.

3.3.2. Kinetic Study

Figure 9 illustrates the comparative reduction of total organic carbon (TOC) during electrolysis using the unmodified Biochar and MOFB@ZnO as a catalyst.

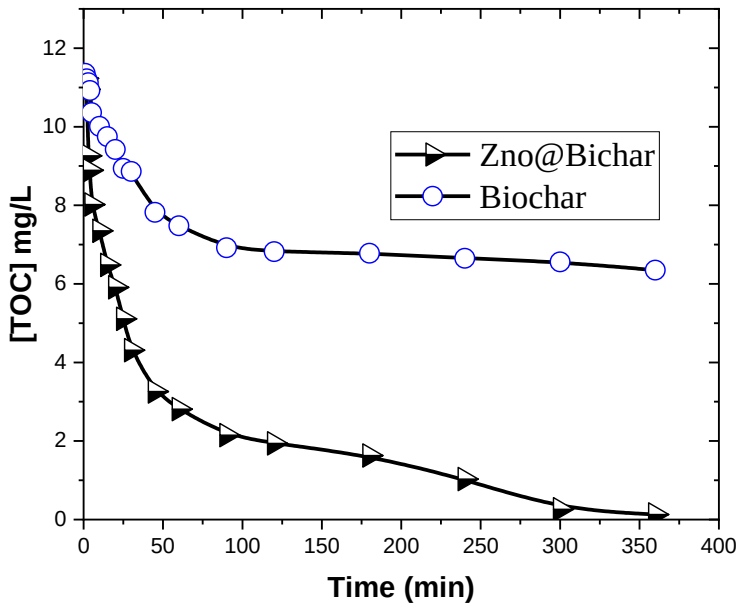

 doi:10.20944/preprints202410.0485.v1

Figure 9. TOC abatement vs electrodegradation time for electrocatalyst/MOFB@ZnO and electrocatalyst/Biochar. For 250 mL of 21mg/L congo-red solution in 0.05M Na_2SO_4 at pH 3 and room temperature, using a Pt/carbon-felt cell at 217 mA.

The TOC measurements show, when unmodified biochar was used, a fall from 11.8 to 10 mg/L accompanied with a discoloration of the solution during the first 30 minutes. This rapid discoloration has been widely observed when using catalysts with azo dyes. Indeed, the complex molecular structure is barely resistant to electro-oxidation; the weakest and first chemical group to be oxidized is the chromophore. The disappearance of the CR color observed during electro-oxidation is due to the rupture of the azo chromophore (-N=N-). This process destroys the conjugated structure responsible for the absorption of visible light and therefore the color. The electrons transferred during electro-oxidation can break this nitrogen-nitrogen double bond, producing free radicals or ions that react with the azo groups to form colorless or differently colored intermediate compounds [81]. Sassi et al. [79,82] concluded that the discoloration may indicate the presence of harmful intermediates, which alone do not sufficiently explain the success of the total dye treatment. Worse, Congo red may be less dangerous than these intermediates. The two main degradation products following the rupture of the N=N bond are 1-naphthylamine-4-sulfonic acid (naphthionic acid) and benzidine [83,84]. These derived aromatic amines are toxic and potentially carcinogenic.

The unmodified catalyst appears to be ineffective in mineralizing the organic compounds within the first 50 minutes, with the TOC measurement stabilizing between 6.5 and 7 mg/L for the duration of the experiment, which lasted approximately 6 hours.

On the other hand, the electrolysis kinetic seems to be enhanced when using the MOFB@ZnO. The rapid degradation, reaching 55% mineralization in the first 25 minutes. However, extended degradation times resulted in a slowdown, with TOC reduced by 98% after 360 minutes.

The electrolysis process has been observed to completely degrade Congo red (CR) into various smaller molecular components. These breakdown products indicate a comprehensive transformation of CR under the electrolysis conditions applied, reflecting the decomposition of its aromatic azo dye structure into simpler, potentially less harmful chemical entities leading to the formation of carbon dioxide (CO_2), water (H_2O), ammonium ions (NH_4^+), nitrate ions (NO_3^-), sulfite ions (SO_3^{2-}). and carboxyl groups (COOH).

3.3.3. Mechanism of Mineralization

With the results obtained in this work and the examination of intermediary products identified by several authors [85–89], we propose a general reaction mechanism for mineralization of azo dye molecules by oxidative action of hydroxyl radicals in the Electro-Fenton process is proposed after refereeing the literature [85–89] (Figure 10). The degradation process appears to occur according to a mechanism proposed by Mansour et al. [90]. The degradation of the dye is more efficient in acidic conditions due to the enhanced sensitivity of the protonated form to the oxidation process.

Preprints.org (www.preprints.org) | NOT PEER-REVIEWED | Posted: 7 October 2024 doi:10.20944/preprints202410.0485.v1

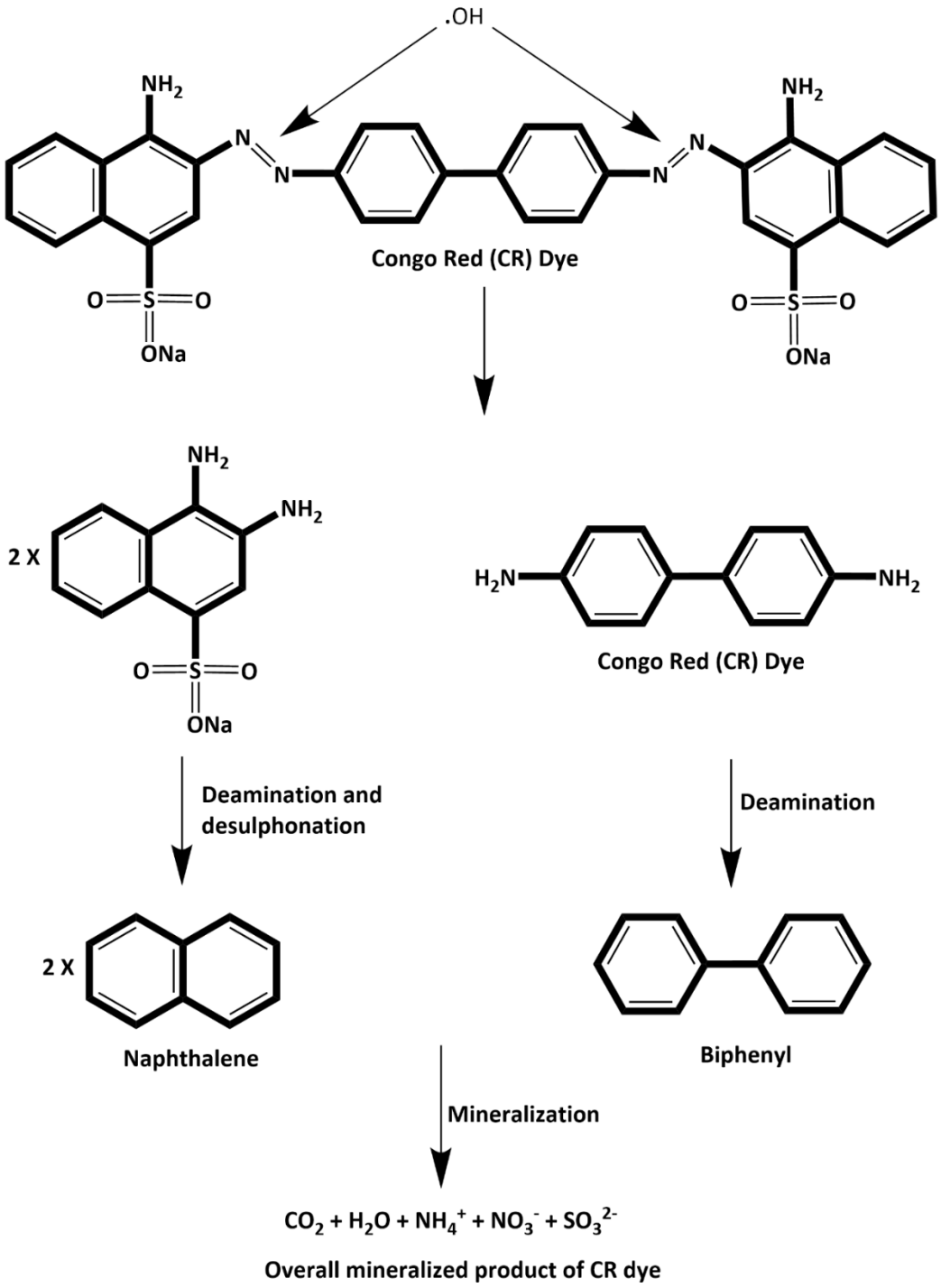

Figure 10. Pathway proposed for the degradation of CR by the electro-Fenton process.

The degradation of organic matter is mainly attributed to the reaction with •OH formed on the surface of the Pt anode [91]. The Zn^{2+} ions were released into the solution. They catalyse the decomposition of H_2O_2, leading to the formation of $^{\cdot}OH$ and Zn^{2+} through a Fenton-like reaction (Eq.9).

For this reaction to occur, Zn^{2+} is first reduced both at the cathode via reaction (Eq.6) and in the solution according to reactions (Eq.7) and at (Eq.8).

$$Zn^{2+} + é \rightarrow Zn^{+} \quad \text{(Eq. 6)}$$

$$Zn^{2+} + H_2O_2 \rightarrow Zn^{+} = HO_2^{\bullet} + H^{+} \quad \text{(Eq. 7)}$$

$$Zn^{2+} + HO_2^{\bullet} \rightarrow Zn^{+} + H^{+} + O_2 \quad \text{(Eq. 8)}$$

$$Zn^{+} + H_2O_2 \rightarrow Zn^{2+} + HO^{\bullet} + OH^{-} \quad \text{(Eq. 9)}$$

 doi:10.20944/preprints202410.0485.v1

For all dyes, decolorization is visually significant for the consumed charge. The electrophilic addition of •OH to the azo double bond leads to its rapid destruction. Studies have detected decolorization through UV-visible spectroscopy. Observing the decrease in the absorption band associated with the –N=N- bond confirms this hypothesis. The compound was converted to 3,4-diaminonaphthalene-1-sulfonate and biphenyl-4,4'-diamine via an oxidation reaction with hydroxyl radicals. This intermediate was transformed into 4-amino-3-hydroxynaphthalene-1-sulfonate, which was oxidized by hydroxyl radicals to produce 4-aminonaphthalene-1-sulfonate. These latter intermediates have been reported in previous studies [92]. Finally, all aromatic intermediates would be oxidized by hydroxyl radicals via ring cleavage reactions to form short-chain aliphatic carboxylic acids, such as 2-hydroxybutanedioic acid, propanedioic acid, acetic acid, and oxaloacetic acid.

3.3.4. Catalyst Mass Effect

The influence of the quantity of MOFB@ZnO on the degradation of CR was studied under optimal mineralization conditions (I = 217 mA, 21 mg/L Congo-red concentration). These results are presented in Figure 11.

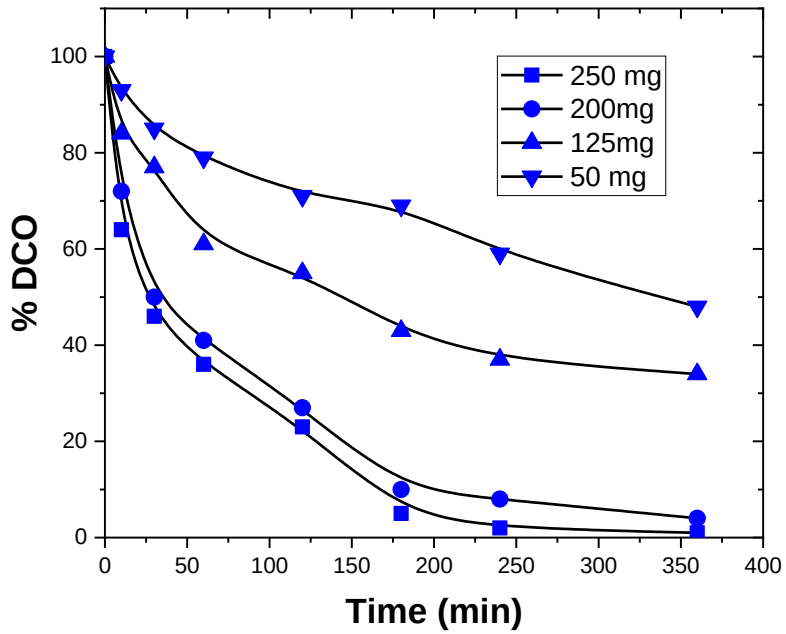

Figure 11. Influence of the catalyst mass on the degradation of an aqueous solution of congo-red. Experimental conditions: For 250 mL of 21mg/L congo-red solution in 0.05M Na_2SO_4 at pH 3 and room temperature, using a Pt/carbon-felt cell at 217 mA.

The CR degradation reaction is very rapid. Indeed, complete decolorization is achieved at around 3 minutes for 250 mg and 200 mg of catalysts, and approximately 8 and 20 minutes for 125 mg and 50 mg, respectively. The degradation of organic compounds significantly depends on the amount of released Zinc, which must be optimized to achieve the best degradation. As shown in Figure 11, the efficiency of degradation increased with the amount of MOFB@ZnO catalyst. The improvement in electrocatalytic degradation performance may be due to the enhanced release of Zn^{2+} ions from the MOFB@ZnO surface, which can increase •OH radicals.

3.3.5. Regeneration of MOFB@ZnO

In practical applications, the stability and reusability of electro-catalysts are paramount. The electro-catalytic degradation experiments were repeated multiple times under consistent conditions. Figure 12 shows the variation in degradation activity of the MOFB@ZnO composite catalysts over five consecutive electrolysis cycles.

Preprints.org (www.preprints.org) | NOT PEER-REVIEWED | Posted: 7 October 2024 doi:10.20944/preprints202410.0485.v1

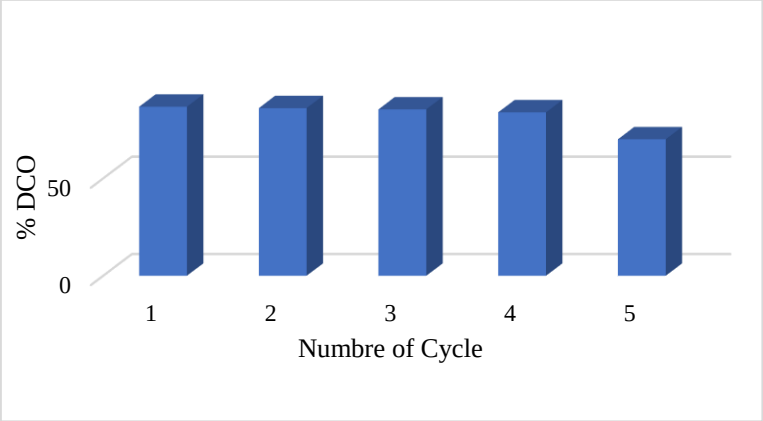

Figure 12. Recycling of the MOFB@ZnO in the electrodegradation of congo-red from aqueous solution.

The results indicate that there was no notable decrease in catalyst activity, affirming the stability and long-term durability of the MOFB@ZnO modified biochar.

Indeed, the recycling of biochar modified with ZnO does not disrupt the electrolysis of Congo red due to their distinct functional roles in the process. Biochar seems to be acting purely as a chemically inert support material, providing a stable platform for the immobilization of ZnO nanoparticles. These nanoparticles, in turn, serve as the active sites for catalytic reactions during electrolysis. Their role involves initiating redox reactions and generating reactive species (such as hydroxyl radicals) essential for the degradation of Congo red as mentioned by Sassi et al. [82].

When, the biochar remains unchanged chemically and mechanically during the process, its recycling does not compromise the catalytic effectiveness of the ZnO nanoparticles. This ensures consistent and efficient performance of the composite material across repeated cycles of use, maintaining its capability to degrade Congo red through electrolysis effectively.

The present methodology was compared with one reported for the Congo red dye degradation and found that this work has superiority over other in terms of degradation efficiency over other methods including the one treated electrochemically as shown in Table 2.

Table 2. Comparison of degradation efficiency of present catalyst with literature.

Name of Catalyst	Synthesis procedure	CR dye conc.	Amount of catalyst	Time/ Conditions	% Degradation	Ref.
Pt/Cu NPs	Electrodeposition	150 ml of 50 mg /L		60 min / Electrochemical	95.95%	[93]
MWCNT-MnO_2/Ni foam	Hydrothermal	500 mL of 100 mg/L		90 min/Electrochemical	92%	[94]
ZnO-biochar (*Ulva lactuca* extract from Algae as a source of biochar)	Hydro-thermal	30 mg/L	0.05 g catalyst/100 mL CR solution	120 min / UV lamp	89.28%	[45]
Aspergillus strains	Fungal strains used isolated from soil	100 mg/L		7 days at 30 °C	More than 86%.	[95]
MWNTS supported Ag–Co oxides	Chemical reduction method	10mL (80 ppm)	0.02g	75 min/UV	90.37%	[96]
TiO_2	Not given	250 ml of 4ppm	0.1g	30 min /UV lamp	66.99%	[97]
MOFB@ZnO (*Moringa oleifera* as a precursor of biochar)	Pyrolysis	250 mL of 20mg/L	0.2 g/L	3 min for complete	98%	This work

 doi:10.20944/preprints202410.0485.v1

			decolourization and 360 min for TOC removal/ electrochemical

4. Conclusions

The present work reports on the utilization of one pot wet impregnation technique to make MOFB@ZnO nanocomposite catalyst. This work is a good example of agricultural biomass waste conversion from trash to biochar (black gold). The applicability of the present material is successfully demonstrated by degrading Congo Red dye electrochemically. This catalyst is highly efficient in obtaining almost total mineralization (98% removal of TOC) of the Congo red solution. This work takes into account the United Nations Sustainable Development Goals 6: clean water and sanitation.

Acknowledgments: A. K. B. is grateful to Wallonie-Bruxelles International Excellence World (N°imputation – 101386, and Article Budgetaire – 33.01.00.07) for post-doctoral fellowship. We thank the technical officers of ITODYS for FESEM, XPS, Raman and XRD analysis. Labex SEAM (ANR-11-LABX-086, ANR-11-IDEX-0502) grant is also acknowledged for their support. The authors thank the China Scholarship Council for the provision of Ph.D. scholarship to M.T (No 202008310221).

Declaration of Competing Interest: Authors declares no competing interest.

References

1. Nasir, S.; Hussein, M.Z.; Zainal, Z.; Yusof, N.A. Carbon-Based Nanomaterials / Allotropes : A Glimpse of Their Synthesis , Properties and Some Applications. *Materials* **2018**, *11*, 295, doi:10.3390/ma11020295.
2. Gęca, M.; Khalil, A.M.; Tang, M.; Bhakta, A.K.; Snoussi, Y.; Nowicki, P.; Wiśniewska, M.; Chehimi, M.M. Surface Treatment of Biochar—Methods, Surface Analysis and Potential Applications: A Comprehensive Review. *Surfaces* **2023**, *6*, 179–213, doi:10.3390/surfaces6020013.
3. Sarker, T.R.; Nanda, S.; Dalai, A.K. Parametric Studies on Hydrothermal Gasification of Biomass Pellets Using Box-Behnken Experimental Design to Produce Fuel Gas and Hydrochar. *Journal of Cleaner Production* **2023**, *388*, 135804, doi:10.1016/j.jclepro.2022.135804.
4. Cibien, L.; Parot, M.; Fotsing, P.N.; Gaveau, P.; Woumfo, E.D.; Vieillard, J.; Napoli, A.; Brun, N. Ionothermal Carbonization in [Bmim][FeCl4]: An Opportunity for the Valorization of Raw Lignocellulosic Agrowastes into Advanced Porous Carbons for CO2 Capture. *Green Chemistry* **2020**, *22*, 5423–5436, doi:DOI https://doi.org/10.1039/D0GC01510E.
5. Sirohi, R.; Vivekanand, V.; Pandey, A.K.; Tarafdar, A.; Awasthi, M.K.; Shakya, A.; Kim, S.H.; Sim, S.J.; Tuan, H.A.; Pandey, A. Emerging Trends in Role and Significance of Biochar in Gaseous Biofuels Production. *Environmental Technology & Innovation* **2023**, *30*, 103100, doi:10.1016/j.eti.2023.103100.
6. Ghogia, A.C.; Millán, L.M.R.; White, C.E.; Nzihou, A. Synthesis and Growth of Green Graphene from Biochar Revealed by Magnetic Properties of Iron Catalyst. *ChemSusChem* **2023**, *16*, e202201864, doi:10.1002/cssc.202201864.
7. Greenough, S.; Dumont, M.-J.; Prasher, S. The Physicochemical Properties of Biochar and Its Applicability as a Filler in Rubber Composites : A Review. *Materials Today Communications* **2021**, *29*, 102912, doi:10.1016/j.mtcomm.2021.102912.
8. Balmuk, G.; Videgain, M.; Manyà, J.J.; Duman, G.; Yanik, J. Effects of Pyrolysis Temperature and Pressure on Agronomic Properties of Biochar. *Journal of Analytical and Applied Pyrolysis* **2023**, *169*, 105858, doi:10.1016/j.jaap.2023.105858.
9. Bhakta, A.K.; Snoussi, Y.; Garah, M. El; Ammar, S.; Chehimi, M.M. Brewer's Spent Grain Biochar : Grinding Method Matters. *Journal of Carbon Research* **2022**, *8*, 46, doi:https://doi.org/10.3390/c8030046.
10. Novotný, M.; Marković, M.; Raček, J.; Šipka, M.; Chorazy, T.; Tošić, I.; Hlavínek, P. The Use of Biochar Made from Biomass and Biosolids as a Substrate for Green Infrastructure: A Review. *Sustainable Chemistry and Pharmacy* **2023**, *32*, 100999, doi:10.1016/j.scp.2023.100999.
11. Peiris, C.; Alahakoon, Y.A.; Malaweera Arachchi, U.; Mlsna, T.E.; Gunatilake, S.R.; Zhang, X. Phosphorus-Enriched Biochar for the Remediation of Heavy Metal Contaminated Soil. *Journal of Agriculture and Food Research* **2023**, *12*, 100546, doi:10.1016/j.jafr.2023.100546.
12. Nogués, I.; Mazzurco Miritana, V.; Passatore, L.; Zacchini, M.; Peruzzi, E.; Carloni, S.; Pietrini, F.; Marabottini, R.; Chiti, T.; Massaccesi, L.; et al. Biochar Soil Amendment as Carbon Farming Practice in a Mediterranean Environment. *Geoderma Regional* **2023**, *33*, e00634, doi:10.1016/j.geodrs.2023.e00634.

13. Roy, H.; Sarkar, D.; Pervez, M.N.; Paul, S.; Cai, Y.; Naddeo, V.; Firoz, S.H.; Islam, M.S. Synthesis, Characterization and Performance Evaluation of Burmese Grape (Baccaurea Ramiflora) Seed Biochar for Sustainable Wastewater Treatment. *Water* **2023**, *15*, 394, doi:10.3390/w15030394.
14. Bayoka, H.; Snoussi, Y.; Bhakta, A.K.; El Garah, M.; Khalil, A.M.; Jouini, M.; Ammar, S.; Chehimi, M.M. Evidencing the Synergistic Effects of Carbonization Temperature, Surface Composition and Structural Properties on the Catalytic Activity of Biochar/Bimetallic Composite. *Journal of Analytical and Applied Pyrolysis* **2023**, *173*, 106069, doi:10.1016/j.jaap.2023.106069.
15. Safarian, S. To What Extent Could Biochar Replace Coal and Coke in Steel Industries? *Fuel* **2023**, *339*, 127401, doi:10.1016/j.fuel.2023.127401.
16. Molaiyan, P.; Dos Reis, G.S.; Karuppiah, D.; Subramaniyam, C.M.; García-Alvarado, F.; Lassi, U. Recent Progress in Biomass-Derived Carbon Materials for Li-Ion and Na-Ion Batteries—A Review. *Batteries* **2023**, *9*, 116, doi:10.3390/batteries9020116.
17. Rawat, S.; Boobalan, T.; Sathish, M.; Hotha, S.; Thallada, B. Utilization of CO2 Activated Litchi Seed Biochar for the Fabrication of Supercapacitor Electrodes. *Biomass and Bioenergy* **2023**, *171*, 106747, doi:10.1016/j.biombioe.2023.106747.
18. J.E., M.; Chandewar, P.R.; Shee, D.; Sankar Mal, S. Phosphomolybdic Acid Embedded into Biomass-Derived Biochar Carbon Electrode for Supercapacitor Applications. *Journal of Electroanalytical Chemistry* **2023**, *936*, 117354, doi:10.1016/j.jelechem.2023.117354.
19. Marchesini, J.; Perondi, D.; Godinho, M.V.M.V.G.P.G.O.C.M.; Piazza, D. Production and Application of Biochar in a UV Radiation-Curable Epoxy Paint as a Substitute for Graphite. *Journal of Coatings Technology and Research* **2023**, doi:https://doi.org/10.1007/s11998-022-00715-w.
20. Ghassemi-Golezani, K.; Farhangi-Abriz, S. Biochar Related Treatments Improved Physiological Performance, Growth and Productivity of Mentha Crispa L. Plants under Fluoride and Cadmium Toxicities. *Industrial Crops and Products* **2023**, *194*, 116287, doi:10.1016/j.indcrop.2023.116287.
21. Amalina, F.; Krishnan, S.; Zularisam, A.W.; Nasrullah, M. Recent Advancement and Applications of Biochar Technology as a Multifunctional Component towards Sustainable Environment. *Environmental Development* **2023**, *46*, 100819, doi:10.1016/j.envdev.2023.100819.
22. Lilli, M.A.; Paranychianakis, N. V.; Lionoudakis, K.; Kritikaki, A.; Voutsadaki, S.; Saru, M.L.; Komnitsas, K.; Nikolaidis, N.P. The Impact of Sewage-Sludge- and Olive-Mill-Waste-Derived Biochar Amendments to Tomato Cultivation. *Sustainability* **2023**, *15*, 3879, doi:10.3390/su15053879.
23. Jha, S.; Gaur, R.; Shahabuddin, S.; Tyagi, I. Biochar as Sustainable Alternative and Green Adsorbent for the Remediation of Noxious Pollutants: A Comprehensive Review. *Toxics* **2023**, *11*, 117, doi:10.3390/toxics11020117.
24. Amalina, F.; Krishnan, S.; Zularisam, A.W.; Nasrullah, M. Biochar and Sustainable Environmental Development towards Adsorptive Removal of Pollutants: Modern Advancements and Future Insight. *Process Safety and Environmental Protection* **2023**, *173*, 715–728, doi:10.1016/j.psep.2023.03.069.
25. Kumar, M.; Ambika, S.; Hassani, A.; Nidheesh, P. V. Waste to Catalyst: Role of Agricultural Waste in Water and Wastewater Treatment. *Science of the Total Environment* **2023**, *858*, 159762, doi:10.1016/j.scitotenv.2022.159762.
26. Elbadawy, H.A.; Elhusseiny, A.F.; Hussein, S.M.; Sadik, W.A. Sustainable and Energy-Efficient Photocatalytic Degradation of Textile Dye Assisted by Ecofriendly Synthesized Silver Nanoparticles. *Scientific Reports* **2023**, *13*, 2302, doi:10.1038/s41598-023-29507-x.
27. Hadadi, A.; Imessaoudene, A.; Bollinger, J.C.; Bouzaza, A.; Amrane, A.; Tahraoui, H.; Mouni, L. Aleppo Pine Seeds (Pinus Halepensis Mill.) as a Promising Novel Green Coagulant for the Removal of Congo Red Dye: Optimization via Machine Learning Algorithm. *Journal of Environmental Management* **2023**, *331*, 117286, doi:10.1016/j.jenvman.2023.117286.
28. Ahmad Aftab, R.; Zaidi, S.; Aslam Parwaz Khan, A.; Arish Usman, M.; Khan, A.Y.; Tariq Saeed Chani, M.; Asiri, A.M. Removal of Congo Red from Water by Adsorption onto Activated Carbon Derived from Waste Black Cardamom Peels and Machine Learning Modeling. *Alexandria Engineering Journal* **2023**, *71*, 355–369, doi:10.1016/j.aej.2023.03.055.
29. Oladoye, P.O.; Bamigboye, M.O.; Ogunbiyi, O.D.; Akano, M.T. Toxicity and Decontamination Strategies of Congo Red Dye. *Groundwater for Sustainable Development* **2022**, *19*, 100844, doi:10.1016/j.gsd.2022.100844.
30. Sachin; Pramanik, B.K.; Singh, N.; Zizhou, R.; Houshyar, S.; Cole, I.; Yin, H. Fast and Effective Removal of Congo Red by Doped ZnO Nanoparticles. *Nanomaterials* **2023**, *13*, 566, doi:10.3390/nano13030566.
31. Okpara, E.C.; Olatunde, O.C.; Wojuola, O.B.; Onwudiwe, D.C. Applications of Transition Metal Oxides and Chalcogenides and Their Composites in Water Treatment: A Review. *Environmental Advances* **2023**, *11*, 100341, doi:10.1016/j.envadv.2023.100341.
32. Han, Y.; Wang, J.; Qi, D. Low-temperature Synthesis of Maize Straw biochar-ZnO Nanocomposites for Efficient Adsorption and Photocatalytic Degradation of Methylene Blue. *ChemistrySelect* **2023**, *8*, e202300511, doi:10.1002/slct.202300511.

33. Abdulrahman, A.F.; Abdulqodus, A.N.; Almessiere, M.A. Biosynthesis of Al-Doped ZnO Nanoparticles with Different Al Doping Ratio for Methylene Orange Dye Degradation Activity. *Ceramics International* **2023**, *49*, 34920–34936, doi:10.1016/j.ceramint.2023.08.165.
34. Salunkhe, T.T.; Kumar, V.; Kadam, A.N.; Mali, M.; Misra, M. Rational Construction of Hollow ZnO@SnS2 Core-Shell Nanorods: A Way to Boost Catalytic Removal of Cr (VI) Ions, Antibiotic and Industrial Dyes. *Ceramics International* **2023**, doi:https://doi.org/10.1016/j.ceramint.2023.10.282.
35. Mahajan, D.S.R.V.A.C.S.K.P.T.V.K.M.S.P.K.A.K. Soapnut Plant–Mediated ZnO and Ag-ZnO Nanoparticles for Environmental and Biological Applications. *emergent mater.* **2023**, doi:https://doi.org/10.1007/s42247-023-00564-2.
36. Chen, X.; Li, Y.; Fei, Y.; Li, Y.; Wang, L.; Xie, A.; Sun, D. Optimization of Photoelectric Properties of Transparent Conductive B and Ga Co-Doped ZnO Films for Electrochromic Applications. *Ceramics International* **2023**, doi:https://doi.org/10.1016/j.ceramint.2023.10.332.
37. Zarate, Raquel.P.L.; Raimundo, R.A.; Medeiros, E.S.; Torquato, R.A. Structural, Morphological, Optical and Thermoresistive Study of the Polyaniline/Polylactic Acid/ZnO Films Produced by Solution Blow Spraying for Temperature Sensors. *Ceramics International* **2023**, doi:https://doi.org/10.1016/j.ceramint.2023.10.053.
38. Zhu, J.; Fan, C.; Ning, C.; Wang, W. Cathodic Electrophoretic Deposited HA-rGO-ZnO Ternary Composite Coatings on ZK60 Magnesium Alloy for Enhanced Corrosion Stability. *Ceramics International* **2023**, *49*, 37604–37622, doi:10.1016/j.ceramint.2023.09.087.
39. Vertepov, A.E.; Fedorova, A.A.; Batkin, A.M.; Knotko, A. V; Maslakov, K.I.; Doljenko, V.D.; Vasiliev, A. V; Kapustin, G.I.; Shatalova, T.B.; Sorokina, N.M.; et al. CO2 Hydrogenation to Methanol on CuO-ZnO/SiO2 and CuO-ZnO/CeO2 -SiO2 Catalysts Synthesized with β -Cyclodextrin Template. *Catalyst* **2023**, *13*, 1231, doi:https://doi.org/10.3390/catal13091231.
40. Gierałtowska, S.; Zaleszczyk, W.; Putkonen, M.; Zasada, D.; Korona, K.P.; Norek, M. Regularly Arranged ZnO / TiO2 , HfO2 , and ZrO2 Core / Shell Hybrid Nanostructures - towards Selection of the Optimal Shell Material for Efficient ZnO-Based UV Light Emitters. *Ceramics International* **2023**, *49*, 31679–31690, doi:10.1016/j.ceramint.2023.07.122.
41. Chauhan, S.; Rai, S.; Pandit, S.; Roy, A.; Gacem, A.; El-hiti, G.A.; Yadav, K.K.; Ravindran, B.; Cheon, J.; Jeon, B. Neodymium-Doped Zinc Oxide Nanoparticles Catalytic Cathode for Enhanced Efficiency of Microbial Desalination Cells. *Catalysts* **2023**, *2*, 1164, doi:https://doi.org/10.3390/catal13081164.
42. Mirzaei, H.; Darroudi, M. Zinc Oxide Nanoparticles_ Biological Synthesis and Biomedical Applications. *Ceramics International* **2017**, *43*, 907–914, doi:10.1016/j.ceramint.2016.10.051.
43. Rubangakene, N.O.; Elwardany, A.; Fujii, M.; Sekiguchi, H.; Elkady, M.; Shokry, H. Biosorption of Congo Red Dye from Aqueous Solutions Using Pristine Biochar and ZnO Biochar from Green Pea Peels. *Chemical Engineering Research and Design* **2023**, *189*, 636–651, doi:10.1016/j.cherd.2022.12.003.
44. Iqbal, M.M.; Imran, M.; Hussain, T.; Naeem, M.A.; Al-Kahtani, A.A.; Shah, G.M.; Ahmad, S.; Farooq, A.; Rizwan, M.; Majeed, A.; et al. Effective Sequestration of Congo Red Dye with ZnO/Cotton Stalks Biochar Nanocomposite: MODELING, Reusability and Stability. *Journal of Saudi Chemical Society* **2021**, *25*, 101176, doi:10.1016/j.jscs.2020.101176.
45. Dumbrava, A.; Matei, C.; Diacon, A.; Moscalu, F.; Berger, D. Novel ZnO-Biochar Nanocomposites Obtained by Hydrothermal Method in Extracts of Ulva Lactuca Collected from Black Sea. *Ceramics International* **2023**, *49*, 10003–10013, doi:10.1016/j.ceramint.2022.11.178.
46. Laxmi Deepak Bhatlu, M.; Athira, P.S.; Jayan, N.; Barik, D.; Dennison, M.S. Preparation of Breadfruit Leaf Biochar for the Application of Congo Red Dye Removal from Aqueous Solution and Optimization of Factors by RSM-BBD. *Adsorption Science and Technology* **2023**, *2023*, doi:https://doi.org/10.1155/2023/7369027.
47. Gopalakrishnan, L.; Doriya, K.; Kumar, D.S. Moringa Oleifera: A Review on Nutritive Importance and Its Medicinal Application. *Food Science and Human Wellness* **2016**, *5*, 49–56, doi:10.1016/j.fshw.2016.04.001.
48. Prasad, B.; Dave, H.; Maurya, D.M.; Singh, D.; Kumari, M.; Prasad, K.S. Sorptive Removal of Aqueous Arsenite and Arsenate Ions onto a Low Cost, Calcium Modified Moringa Oleifera Wood Biochar (CaMBC). *Environmental Quality Management* **2022**, *31*, 461–468, doi:10.1002/tqem.21831.
49. Gourai, M.; Nayak, A.K.; Nial, P.S.; Satpathy, B.; Bhuyan, R.; Singh, S.K.; Subudhi, U. Thermal Plasma Processing of Moringa Oleifera Biochars: Adsorbents for Fluoride Removal from Water. *RSC Advances* **2023**, *13*, 4340–4350, doi:10.1039/d2ra07514h.
50. Raji, Y.; Nadi, A.; Mechnou, I.; Saadouni, M.; Cherkaoui, O.; Zyade, S. High Adsorption Capacities of Crystal Violet Dye by Low-Cost Activated Carbon Prepared from Moroccan Moringa Oleifera Wastes: Characterization, Adsorption and Mechanism Study. *Diamond and Related Materials* **2023**, *135*, 109834, doi:10.1016/j.diamond.2023.109834.
51. Roy, H.; Islam, M.S.; Arifin, M.T.; Firoz, S.H. Chitosan-ZnO Decorated Moringa Oleifera Seed Biochar for Sequestration of Methylene Blue: Isotherms, Kinetics, and Response Surface Analysis. *Environmental Nanotechnology, Monitoring and Management* **2022**, *18*, 100752, doi:10.1016/j.enmm.2022.100752.

52. Abad, S.S.A.M.K.; Javidan, P.; Baghdadi, M.; Mehrdadi, N. Green Synthesis of Pd@biochar Using the Extract and Biochar of Corn-Husk Wastes for Electrochemical Cr(VI) Reduction in Plating Wastewater. *Journal of Environmental Chemical Engineering* **2023**, *11*, 109911, doi:10.1016/j.jece.2023.109911.
53. Liu, Q.; Jiang, S.; Su, X.; Zhang, X.; Cao, W.; Xu, Y. Role of the Biochar Modified with ZnCl2 and FeCl3 on the Electrochemical Degradation of Nitrobenzene. *Chemosphere* **2021**, *275*, 129966, doi:10.1016/j.chemosphere.2021.129966.
54. Guo, L.; Zhao, L.; Tang, Y.; Zhou, J.; Shi, B. An Iron–Based Biochar for Persulfate Activation with Highly Efficient and Durable Removal of Refractory Dyes. *Journal of Environmental Chemical Engineering* **2022**, *10*, 106979, doi:10.1016/j.jece.2021.106979.
55. Lu, Y.; Feng, M.; Wang, Y. Enhancing the Heterogeneous Electro-Fenton Degradation of Methylene Blue Using Sludge-Derived Biochar-Loaded Nano Zero-Valent Iron. *Journal of Water Process Engineering* **2024**, *59*, 104980, doi:10.1016/j.jwpe.2024.104980.
56. Bhakta, A.K.; Tang, M.; Snoussi, Y.; Khalil, A.M.; Mascarenhas, R.J.; Mekhalif, Z.; Abderrabba, M.; Ammar, S.; Chehimi, M.M. Sweety , Salty , Sour , and Romantic Biochar - Supported ZnO : Highly Active Composite Catalysts for Environmental Remediation. *Emergent Materials* **2023**, doi:10.1007/s42247-023-00599-5.
57. Gholami, P.; Dinpazhoh, L.; Khataee, A.; Orooji, Y. Sonocatalytic Activity of Biochar-Supported ZnO Nanorods in Degradation of Gemifloxacin: Synergy Study, Effect of Parameters and Phytotoxicity Evaluation. *Ultrasonics Sonochemistry* **2019**, *55*, 44–56, doi:10.1016/j.ultsonch.2019.03.001.
58. Mankomal; Kaur, H. Synergistic Effect of Biochar Impregnated with ZnO Nano-Flowers for Effective Removal of Organic Pollutants from Wastewater. *Applied Surface Science Advances* **2022**, *12*, 100339, doi:10.1016/j.apsadv.2022.100339.
59. Luyen, N.T.; Nguyen, K. Van; Dang, N. Van; Huy, T.Q.; Linh, P.H.; Trung, N.T.; Nguyen, V.-T.; Thanh, D. Van Facile One-Step Pyrolysis of ZnO/Biochar Nanocomposite for Highly Efficient Removal of Methylene Blue Dye from Aqueous Solution. *ACS Omega* **2023**, *8*, 26816–26827, doi:10.1021/acsomega.3c01232.
60. Hu, Ji.I.; Ma, W.; Pan, Y.; Chen, Z.; Zhang, Z.; Wan, C.; Sun, Y.; Qiu, C. Resolving the Tribo-Catalytic Reaction Mechanism for Biochar Regulated Zinc Oxide and Its Application in Protein Transformation. *Journal of Colloid and Interface Science* **2022**, *607*, 1908–1918, doi:10.1016/j.jcis.2021.09.161.
61. Bekele, E.T.; Sintayehu, Y.D.; Gonfa, B.A.; Sabir, F.K.; Shumete, M.K.; Ravikumar, C.R.; Kumar, N.; Murthy, H.C.A. Green Synthesis of Ternary ZnO/ZnCo2O4 Nanocomposites Using Ricinus Communis Leaf Extract for the Electrochemical Sensing of Sulfamethoxazole. *Inorganic Chemistry Communications* **2024**, *160*, 111964, doi:10.1016/j.inoche.2023.111964.
62. Soares, K.S.N.T.; Nascimento, S.Q.; Mazzetto, S.E.; Ribeiro, V.G.P.; Mele, G.; Carbone, L.; Luz, R.A.S.; Gerôncio, E.T.S.; Cantanhêde, W. Structural, Photoluminescent and Electrochemical Properties of Self-Assembled Co3[Co(CN)6]2/ZnO Nanocomposite. *Inorganica Chimica Acta* **2023**, *551*, 121473, doi:10.1016/j.ica.2023.121473.
63. Ozturk, D.; Gülcan, M. Synthesis, Characterization, and in-Situ H2O2 Generation Activity of Activated Carbon/Goethite/Fe3O4/ZnO for Heterogeneous Electro-Fenton Degradation of Organics from Woolen Textile Wastewater. *Journal of Industrial and Engineering Chemistry* **2023**, *122*, 251–263, doi:10.1016/j.jiec.2023.02.026.
64. Albertsson, J.; Abrahams, S.C.; Kvick, Å. Atomic Displacement, Anharmonic Thermal Vibration, Expansivity and Pyroelectric Coefficient Thermal Dependences in ZnO. *Acta Crystallographica Section B* **1989**, *45*, 34–40, doi:https://doi.org/10.1107/S0108768188010109.
65. Donnay, G.; Kihara, K. . *Powder Diffraction* **1986**, *1*, 64–77.
66. Schulz, H.; K.H.Thiemann Structure Parameters and Polarity of the Wurtzite Type Compounds Sic—2H and ZnO. *Solid State Communications* **1979**, *32*, 783–785, doi:https://doi.org/10.1016/0038-1098(79)90754-3.
67. Thomas, D.; Fernandez, N.B.; Mullassery, M.D.; Surya, R. Biochar-ZnO/Polyaniline Composite in Energy Storage Application: Synthesis, Characterization and Electrochemical Analysis. *Results in Chemistry* **2023**, *6*, 101061, doi:10.1016/j.rechem.2023.101061.
68. Alves, Z.; Brites, P.; Ferreira, N.M.; Figueiredo, G.; Otero-Irurueta, G.; Gonçalves, I.; Mendo, S.; Ferreira, P.; Nunes, C. Thermoplastic Starch-Based Films Loaded with Biochar-ZnO Particles for Active Food Packaging. *Journal of Food Engineering* **2024**, *361*, 111741, doi:10.1016/j.jfoodeng.2023.111741.
69. Yoshizawa, Y.; Ametani, A.; Tsunehiro, J.; Nomura, K.; Itoh, M.; Fukui, F.; Kaminogawa, S. Macrophage Stimulation Activity of the Polysaccharide Fraction from a Marine Alga (Porphyra Yezoensis): Structure-Function Relationships and Improved Solubility. *Bioscience, Biotechnology, and Biochemistry* **1995**, *59*, 1933–1937, doi:https://doi.org/10.1271/bbb.59.1933.
70. Bera, S.; Dhara, S.; Velmurugan, S.; Tyagi, A.K. Analysis on Binding Energy and Auger Parameter for Estimating Size and Stoichiometry of ZnO Nanorods. *International Journal of Spectroscopy* **2012**, *2012*, 1–4, doi:10.1155/2012/371092.
71. Deroubaix, G.; Marcus, P. X-Ray Photoelectron Spectroscopy Analysis of Copper and Zinc Oxides and Sulphides. *Surface and Interface Analysis* **1992**, *18*, 39–46, doi:10.1002/sia.740180107.

72. Dake, L.S.; Baer, D.R.; Zachara, J.M. Auger Parameter Measurements of Zinc Compounds Relevant to Zinc Transport in the Environment. *Surface and Interface Analysis* **1989**, *14*, 71–75, doi:10.1002/sia.740140115.
73. Tagliaferro, A.; Rovere, M.; Padovano, E.; Bartoli, M.; Mauro, G. Introducing the Novel Mixed Gaussian-Lorentzian Lineshape in the Analysis of the Raman Signal of Biochar. *Nanomaterials* **2020**, *10*, 1748, doi:doi:10.3390/nano10091748.
74. Tang, M.; Snoussi, Y.; Bhakta, A.K.; El Garah, M.; Khalil, A.M.; Ammar, S.; Chehimi, M.M. Unusual, Hierarchically Structured Composite of Sugarcane Pulp Bagasse Biochar Loaded with Cu/Ni Bimetallic Nanoparticles for Dye Removal. *Environmental Research* **2023**, *232*, 116232, doi:10.1016/j.envres.2023.116232.
75. Naydenova, I.; Radoykova, T.; Petrova, T.; Sandov, O.; Valchev, I. Utilization Perspectives of Lignin Biochar from Industrial Biomass Residue. *Molecules* **2023**, *28*, 4842, doi:10.3390/molecules28124842.
76. Gonçalves, N.P.F.; Lourenço, M.A.O.; Baleuri, S.R.; Bianco, S.; Jagdale, P.; Calza, P. Biochar Waste-Based ZnO Materials as Highly Efficient Photocatalysts for Water Treatment. *Journal of Environmental Chemical Engineering* **2022**, *10*, 107256, doi:10.1016/j.jece.2022.107256.
77. Ergan, B.T.; Aydin, E.S.; Gengec, E. Improving Electro-Fenton Degradation Performance Using Waste Biomass-Derived-Modified Biochar Electrodes : A Real Environment Textile Water Treatment. *Journal of Environmental Chemical Engineering* **2023**, *11*, 111439, doi:10.1016/j.jece.2023.111439.
78. Prediction and Optimization of Electroplated Ni-Based Coating Composition and Thickness Using Central Composite Design and Artificial Neural Network. *Journal of Applied Electrochemistry* **2021**, *51*, 1591–1604, doi:https://doi.org/10.1007/s10800-021-01602-9.
79. Sassi, W.; Msaadi, R.; Ardhaoui, N.; Ammar, S.; Nafady, A. Selective/Simultaneous Batch Adsorption of Binary Textile Dyes Using Amorphous Perlite Powder: Aspects of Central Composite Design Optimization and Mechanisms. *Journal of Environmental Health Science and Engineering* **2023**, *21*, 441–454, doi:https://doi.org/10.1007/s40201-023-00870-1.
80. Ghanmi, I.; Sassi, W.; Oulego, P.; Collado, S.; Ghorbal, A.; Díaz, M. Optimization and Comparison Study of Adsorption and Photosorption Processes of Mesoporous Nano-TiO 2 during Discoloration of Indigo Carmine Dye. *Microporous and Mesoporous Materials* **2022**, *342*, 112138, doi:10.1016/j.micromeso.2022.112138.
81. Akoulih, M.; Tigani, S.; Byoud, F.; Rharib, M.E.; Saadane, R.; Pierre, S.; Chehri, A.; Ghachtouli, S.E. Electrocoagulation-Based AZO DYE (P4R) Removal Rate Prediction Model Using Deep Learning. *Procedia Computer Science* **2024**, *236*, 51–58, doi:10.1016/j.procs.2024.05.003.
82. Sassi, W.; Ghanmi, I.; Oulego, P.; Collado, S.; Ammar, S.; Díaz, M. Pomegranate Peel-Derived Biochar as Ecofriendly Adsorbent of Aniline-Based Dyes Removal from Wastewater. *Clean Techn Environ Policy* **2023**, *25*, 2689–2705, doi:10.1007/s10098-023-02522-2.
83. Makhtar, S.N.N.M.; Yusof, N.; Fajrina, N.; Hairom, N.H.H.; Aziz, F.; Wan Salleh, W.N. V2O5/Cds as Nanocomposite Catalyst for Congo Red Dye Photocatalytic Degradation under Visible Light. *Materials Today: Proceedings* **2024**, *96*, 69–72, doi:10.1016/j.matpr.2023.10.152.
84. Gaur, J.; Vikrant, K.; Kim, K.-H.; Kumar, S.; Pal, M.; Badru, R.; Masand, S.; Momoh, J. Photocatalytic Degradation of Congo Red Dye Using Zinc Oxide Nanoparticles Prepared Using Carica Papaya Leaf Extract. *Materials Today Sustainability* **2023**, *22*, 100339, doi:10.1016/j.mtsust.2023.100339.
85. Arumugam, B.; Muthukutty, B.; Chen, S.M.; Amanulla, B.; Ramaraj, S.K. Sustainable One-Pot Synthesis of Strontium Phosphate Nanoparticles with Effective Charge Carriers for the Photocatalytic Degradation of Carcinogenic Naphthylamine Derivative. *New Journal of Chemistry* **2021**, *45*, 15437–15447, doi:10.1039/d1nj02231h.
86. Victor, H.; Ganda, V.; Kiranadi, B.; Pinontoan, R. Metabolite Identification from Biodegradation of Congo Red by Pichia Sp. *KnE Life Sciences* **2020**, *2020*, 102–110, doi:10.18502/kls.v5i2.6443.
87. Bhagwat, U.O.; Wu, J.J.; Asiri, A.M.; Anandan, S. Photocatalytic Degradation of Congo Red Using PbTiO3 Nanorods Synthesized via a Sonochemical Approach. *ChemistrySelect* **2018**, *3*, 11851–11858, doi:10.1002/slct.201802303.
88. Maruthapandi, M.; Saravanan, A.; Manohar, P.; Luong, J.H.T.; Gedanken, A. Photocatalytic Degradation of Organic Dyes and Antimicrobial Activities by Polyaniline–Nitrogen-Doped Carbon Dot Nanocomposite. *Nanomaterials* **2021**, *11*, 1128, doi:10.3390/nano11051128.
89. Dong, Y.; Wang, Z.; Yang, X.; Zhu, M.; Chen, R.; Lu, B.; Liu, H. Adsorption and Degradation of Congo Red on a Jarosite-Type Compound. *RSC Advances* **2016**, *6*, 102972–102978, doi:10.1039/c6ra19125h.
90. Mansour, D.; Alblawi, E.; Alsukaib, A.K.D.; Al Shammari, B. Removal of Congo Red Dye by Electrochemical Advanced Oxidation Process : Optimization , Degradation Pathways , and Mineralization. *Sustainable Water Resources Management* **2024**, *10*, 1–10, doi:10.1007/s40899-023-01022-x.
91. Barhoumi, N.; Labiadh, L.; Oturan, M.A.; Oturan, N.; Gadri, A.; Ammar, S.; Brillas, E. Electrochemical Mineralization of the Antibiotic Levofloxacin by Electro-Fenton-Pyrite Process. *Chemosphere* **2015**, *141*, 250–257, doi:10.1016/j.chemosphere.2015.08.003.
92. Yashni, G.; Al-gheethi, A.; Maya, R.; Radin, S.; Dai-viet, N.V.; Al-kahtani, A.A.; Al-sahari, M.; Jihan, N.; Hazhar, N.; Noman, E.; et al. Bio-Inspired ZnO NPs Synthesized from Citrus Sinensis Peels Extract for

 doi:10.20944/preprints202410.0485.v1

Congo Red Removal from Textile Wastewater via Photocatalysis : Optimization , Mechanisms , Techno-Economic Analysis. *Chemosphere* **2021**, *281*, 130661, doi:10.1016/j.chemosphere.2021.130661.

93. Ganash, A.; Alajlani, L.; Ganash, E.; Al-Moubaraki, A. Efficient Electrochemical Degradation of Congo Red Dye by Pt/CuNPs Electrode with Its Attractive Performance, Energy Consumption, and Mechanism: Experimental and Theoretical Approaches. *Journal of Water Process Engineering* **2023**, *56*, 104497, doi:10.1016/j.jwpe.2023.104497.
94. Zhu, H.; Chen, Z. Preparation of MWCNT-MnO2/Ni Foam Composite Electrode for Electrochemical Degradation of Congo Red Wastewater. *International Journal of Electrochemical Science* **2021**, *16*, 1–12, doi:10.20964/2021.05.19.
95. Ameen, F.; Dawoud, T.M.; Alshehrei, F.; Alsamhary, K.; Almansob, A. Decolorization of Acid Blue 29, Disperse Red 1 and Congo Red by Different Indigenous Fungal Strains. *Chemosphere* **2021**, *271*, 129532, doi:10.1016/j.chemosphere.2021.129532.
96. Zada, N.; Khan, I.; Shah, T.; Gul, T.; Khan, N.; Saeed, K. Ag–Co Oxides Nanoparticles Supported on Carbon Nanotubes as an Effective Catalyst for the Photodegradation of Congo Red Dye in Aqueous Medium. *Inorganic and Nano-Metal Chemistry* **2020**, *50*, 333–340, doi:10.1080/24701556.2020.1713159.
97. Harun, N.H.; Rahman, M.N.A.; Kamarudin, W.F.W.; Irwan, Z.; Muhammud, A.; Akhir, N.E.F.M.; Yaafar, M.R. Photocatalytic Degradation of Congo Red Dye Based on Titanium Dioxide Using Solar and UV Lamp. *J Fundam Appl Sci* **2018**, *10*, 832–846.